Piecewise Affine Modelling of Wound-Rotor Synchronous Machines for Real-Time Motor Control

Bernard Steyaert, *Student Member, IEEE*, Ethan Swint, *Member, IEEE*, W. Wesley Pennington, *Member, IEEE*, Matthias Preindl, *Senior Member, IEEE*,

***Abstract*—High-performance control of Wound Rotor Synchronous Machines (WRSM) motor drives requires a nonlinear magnetic model that captures magnetic saturation and cross saturation. This research proposes a generalized Piece-wise Affine (PWA) magnetic and state-space model that divides the current and flux space into simplices. PWA functions are obtained from experimental or Finite Element Analysis (FEA) data leveraging the Delaunay triangulation. Error margins and memory requirements can be optimized for given applications by varying the number of PWA functions. The PWA domains can be irregular and an algorithm to optimize accuracy for a given number of PWA domains is proposed. The PWA performance is compared with a high-fidelity magnetic model. Irregular PWA functions have lower error than regularly gridded tables at reduced size: average error is improved from 15% to 1%; peak error is improved from 20% to 9%. Finally, the PWA state-space model is validated on an experimental testbench with a real-time Micro-Controller Unit (MCU). The state space equations are verified using steady-state and dynamic tests.**

***Index Terms*—Flux estimation, Motor Parameters, Piecewise Linear Techniques, Wound Rotor Synchronous Machine (WRSM).**

I. Introduction

Electric machines produce torque by combining armature current and magnetic flux linkage. This research focuses on the wound rotor synchronous machine (WRSM) that produces the main magnetic field with a rotor winding. WRSMs are a class of electric machines used in power generation, traction (e.g., electric vehicles, EVs), and other industrial and residential applications. They are used as both drives and generators, and are sometimes also referred to as wound field synchronous machines (WFSM), among other names (WFSG, WRSG, RRSM, RRSG, EESM). They have several advantages over PMSMs including: higher level of controllability due to their ability to modulate rotor flux, a large constant-power speed range, and increased cost-effectiveness given that no expensive, rare-earth magnets are required in production. Additionally, the rotor flux can be controlled to correct the power factor of the machine, which can lower the volt-amp (VA) rating on the system inverter [1]. This modulation can also be used to increase the stator current required for low speed, high torque operation, a feature advantageous for reducing cost in electric vehicles (EVs) [2]. For decades WRSMs have been used in power generation (10 MVA - 2200 MVA) [2], [3], while more recently it has proved its effectiveness in the EV space. The Renault Zoe vehicle has used WRSMs since 2012 [4].

However, WRSMs have certain drawbacks when compared to PMSMs including: higher copper losses due to the added rotor windings, and increased mechanical complexity. Brushes and slip rings limit power flow to the rotor (hence power density) due to thermal constraints, although there are designs utilizing wireless power transfer [5]. Finally, WRSM have a strong (nonlinear) coupling between the direct (d) and rotor (r) dimension. This coupling tends to require accurate models and is shown in Fig. 1 and Fig. 2.

Electric machines use ferromagnetic materials to maximize and channel magnetic flux. Modern machines aim at minimizing core materials to reduce motor weight and cost. Such machines tend to operate non-linear magnetic regime in general and exhibit saturation and cross saturation [5]–[13]. The relationship between current and flux linkage is modeled using Magnetic Models (MM) that are also also referred to as flux linkage maps in literature. Such maps tend to be linearized and expressed as inductances or transfer functions for motor control. All controllers use an explicit or implicit MM and control performance depends on the MM accuracy, type of machine, and application [14], [15].

There has been extensive study for MMs which can be categorized into static (offline) and dynamic (online) methods and can include other nonlinear drive-system effects such as switching harmonics and dead times [11], [13], [14], [16], iron losses [13], [14], and machine temperature [13], [14], [16]. Offline MM use one or a combination of Finite Element Analysis (FEA) [8], [11], [16], analytical calculations [7], [8], experimental values [6]–[8], [11], [13]–[16], and current or flux estimation [12], [17] to measure inductances at various operating points. The discrete values obtained by these methods are linked together using a variety of methods, summarized in TABLE I. Online MM use a combination of online-estimated parameters from real-time measurements and an offline MM to produce a

B. Steyaert and M. Preindl are with the Department of Electrical Engineering, Columbia University in the City of New York, New York, NY 10027, USA (e-mail: bernard.steyaert@columbia.edu; matthias.preindl@columbia.edu).

E.B. Swint and W.W. Pennington are with Tau Motors, Inc., Redwood City, CA 94063, USA (email: ethan@taumotors.com; wesley@taumotors.com).

Color versions of one or more of the figures in this paper are available online at http://ieeexplore.ieee.org.

TABLE I: Summary of Offline MM Linking Methods

Type of Link	Linear	Bidirectional	Continuous	Differentiable	Saturation	Cross-sat.
Linearized Inductance	•	•	•	•		
Linearly Interpolated LUT			•		•	•
Hermite and Spline LUT [16], [14], [15]			•	•	•	•
Polynomial Functions [11], [13]			•	•	•	•
Piece-wise Nonlinear Functions [6]			•	•	•	•
Other Nonlinear Functions [7], [8]			•	•	•	•
Piece-wise Linear (PWA)	•	•	•		•	•

dynamic MM. This MM model has the ability to adapt to temperature, switch dead time, PWM harmonics, aging, and partial faults in real time. Some online estimation techniques include Extended Kalman Filters [18], neural networks [17], and Taylor Series approximations [12]. Both MM methods are subject to computational and memory constraints of the Digital Signal Processor (DSP), which is used for control. The majority of WRSM controllers use offline MM such as in sliding mode control [3], maximum torque [19], passivity-based control [1], and predictive control [20]. However, some WRSM controllers with online MM have been studied using PI control [10] and deadbeat control [12]. All of these controllers use a linear inductance MM, which does not capture saturation.

This research introduces a MM expressed as Piecewise Affine (PWA) functions and derives a PWA state-space model for WRSMs. The approach has the potential to capture any saturation effects and can be generalized to any motor type. This paper is organized as follows. The WRSM dynamic model using PWA is presented in Section II. Formalization of the PWA functions between a current and flux space and a method of dividing a large datasets is described in Section III and IV respectively. Static evaluation and performance on a DSP is shown in Section V, dynamic evaluation using a WRSM bench setup is demonstrated in Section VI, and Section VII is the conclusion.

II. WRSM Model

The three-phase WRSM can be described dynamically as a state-space model [21]. For formal simplicity and the common challenges of displaying spaces higher than three, this research focuses on the most common WRSM used in

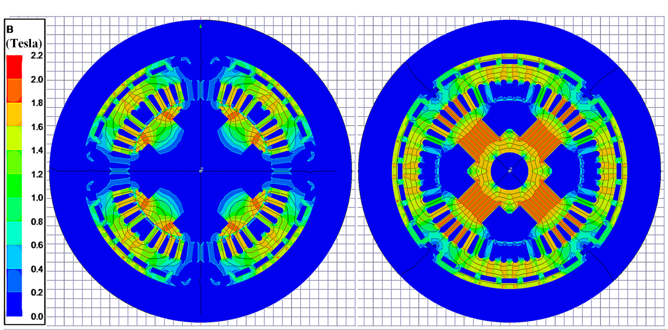

Fig. 1: WRSM cross section showing a saturated flux density B distribution in Tesla at $i_q = 1$ pu (left), and $i_d = 1$ pu (right)

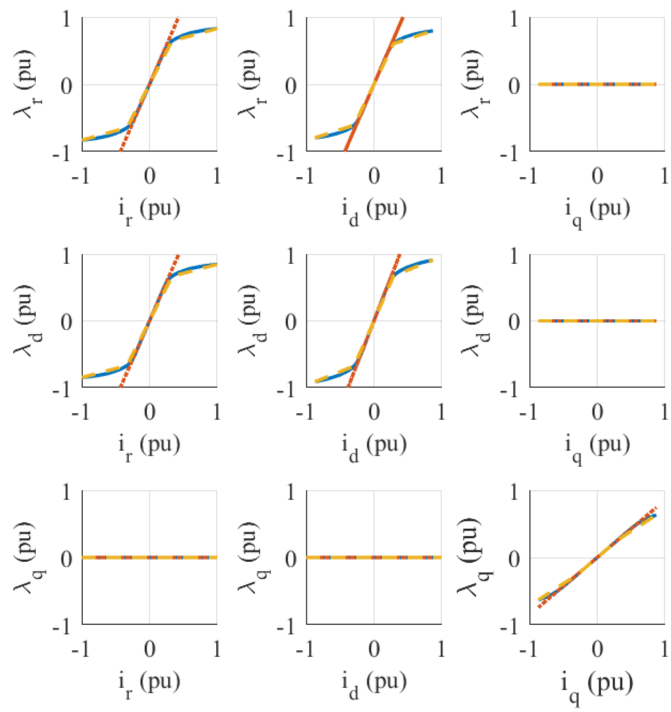

Fig. 2: WRSM flux vs current: experimental (blue), example linearization through origin (orange), example of three-segment PWA (yellow)

motor drives: a neutral-point isolated machine (without zero-axis flux and current) and without damper windings. The equations to adopt this method for more variables (zero-sequence current, damper windings) can be extended using higher dimensions [22].

The voltage equations of the WRSM are [12], [23]

$$\dot{\lambda}_r = u_r - R_r i_r \qquad = \bar{u}_r, \tag{1a}$$

$$\dot{\lambda}_d = \omega\lambda_q + u_d - R_s i_d \qquad = \omega\lambda_q + \bar{u}_d, \tag{1b}$$

$$\dot{\lambda}_q = -\omega\lambda_d + u_q - R_s i_q \qquad = -\omega\lambda_d + \bar{u}_q, \tag{1c}$$

where $\dot{}$ is the $\frac{d}{dt}$ operator; λ_r is the rotor, i.e. field, flux linkage; λ_d, and λ_q are the d-axis and q-axis stator flux linkages respectively; i and u are the currents and voltages of the appropriate dimension; R_r and R_s are the rotor and stator resistances; ω is the synchronous speed, i.e. the electrical velocity of the machine.

Furthermore, we introduce the voltages $\bar{u}$ that are the terminal voltages compensated by the winding resistive voltage drop. This concept can be generalized to include compensation for inverter nonlinear behavior such as

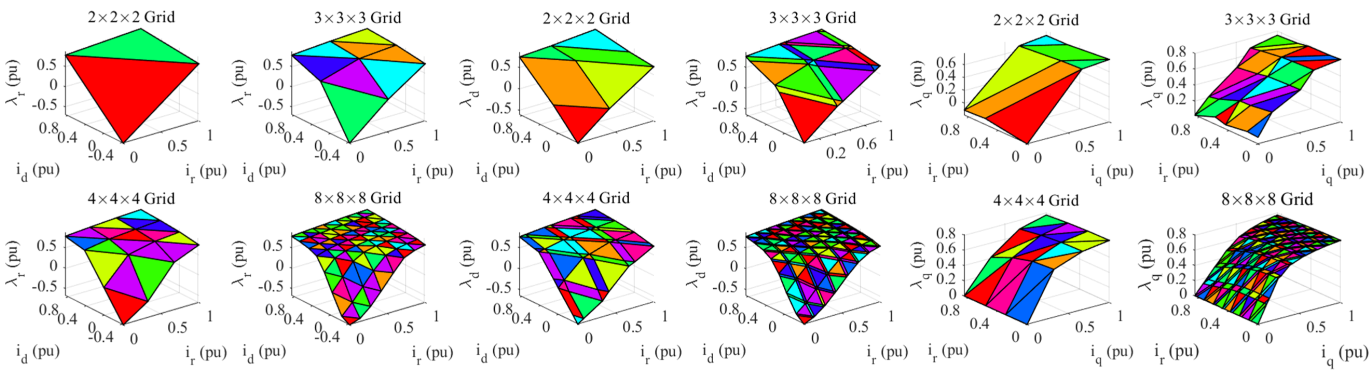

Fig. 3: PWA using $3 \times 3 \times 3$, $4 \times 4 \times 4$, $5 \times 5 \times 5$ and $8 \times 8 \times 8$ regularly sampled current grids: (left) λ_r vs i_d and i_d sliced at $i_q = 0$ pu, (middle) λ_d vs i_r and i_d sliced at $i_q = 0$ pu, (right) λ_q vs i_q and i_r sliced at $i_d = 0$ pu.

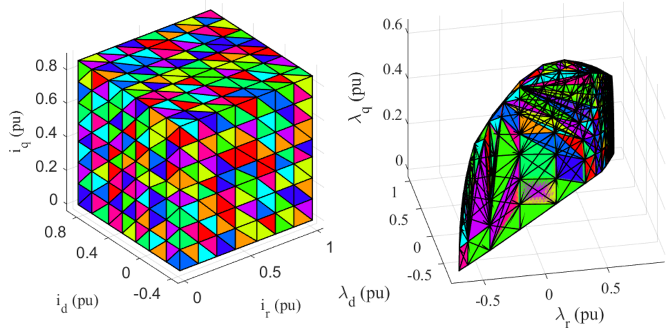

Fig. 4: Mesh of simplices $\mathcal{I}_j \in \mathcal{I}_M$ in current space (left), and mesh of simplices $\Lambda_j \in \Lambda_M$ (right) in flux space

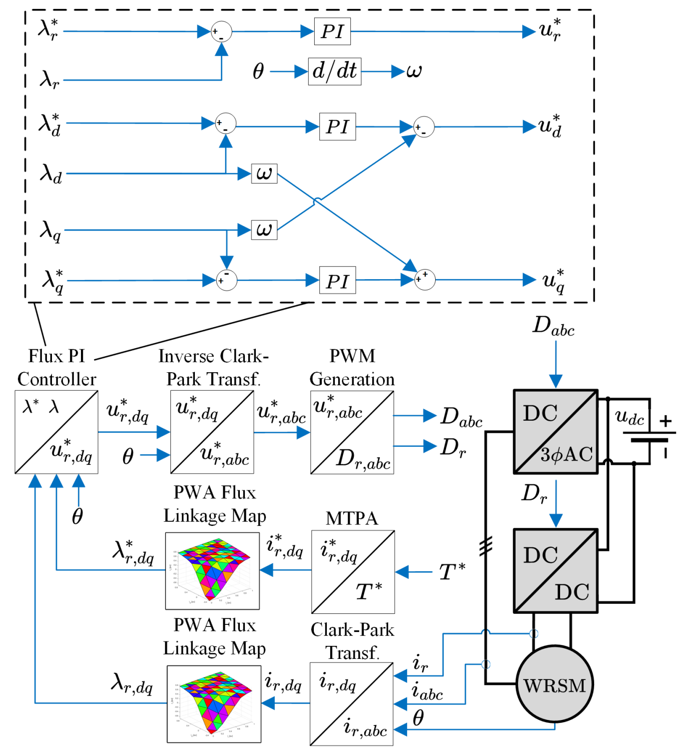

Fig. 5: Reference implementation of a WRSM motor drive (gray) with motor controller using PWA current-flux maps (white)

switch on-voltage drops and dead-times [11], [24]. These effects and space harmonics, such as slotting effects, are not included in this model, however can be included by adding a fourth spatial dependency (position) to the model. It is later shown in Section VI that the model is sufficiently accurate even without these effects included.

The power-invariant Clarke transformation is used and the magnetic axis of the field winding is the reference angle of the Park transformation. In this framework, the machine torque is

$$T = pi'\mathbf{J}\lambda, \tag{2}$$

where p is the number of pole pairs, the flux is $\lambda = [\lambda_r, \lambda_d, \lambda_q]^T \in \Lambda$, the current is $i = [i_r, i_d, i_q]^T \in \mathcal{I}$, and $\mathbf{J}$ is the cross coupling matrix

$$\mathbf{J} = \begin{bmatrix} 0 & 0 & 0 \\ 0 & 0 & -1 \\ 0 & 1 & 0 \end{bmatrix}. \tag{3}$$

The machine currents map onto machine flux with a nonlinear map [21]

$$\lambda_r = f_r(i_r, i_d, i_q), \tag{4a}$$
$$\lambda_d = f_d(i_r, i_d, i_q), \tag{4b}$$
$$\lambda_q = f_q(i_r, i_d, i_q), \tag{4c}$$

that captures magnetic coupling between axis, magnetic saturation, and cross-saturation.

These equations can be written as a standard state-space systems using vector notation

$$\dot{\lambda} = \mathbf{A}\lambda + \mathbf{B}\bar{u}, \tag{5a}$$
$$i = g(\lambda), \tag{5b}$$

where the state is the flux λ, the input is the compensated voltage $\bar{u} = [\bar{u}_r, \bar{u}_d, \bar{u}_q]^T \in \mathcal{U}$, and the measurement is the current i. The linear dynamic model is defined by the matrices

$$\mathbf{A} = \begin{bmatrix} 0 & 0 & 0 \\ 0 & 0 & \omega \\ 0 & -\omega & 0 \end{bmatrix}, \quad \mathbf{B} = \mathbf{I} = \begin{bmatrix} 1 & 0 & 0 \\ 0 & 1 & 0 \\ 0 & 0 & 1 \end{bmatrix}. \tag{6}$$

The output function $g : \lambda \to i$ is the inverse of the nonlinear flux map $f(\cdot) = [f_r(\cdot), f_d(\cdot), f_q(\cdot)]^T$

$$f : i \to \lambda. \tag{7}$$

The map $f(\cdot)$ is typically obtained with finite element analysis (FEA) or through experimental measurement campaigns. This approach describes the map $f(\cdot)$ by N tuples of current i_j and flux linkage λ_j with $j \in \{0, 1, \ldots, N\}$. The sets of points containing all measurements $\mathcal{I}_P = \{i_1, \ldots, i_N\} \subset \mathcal{I}$ and $\Lambda_P = \{\lambda_1, \ldots, \lambda_N\} \subset \Lambda$ are assumed to be in a general position to define a lookup table (LUT) that approximates the map $f(\cdot)$. The data is typically ordered in the first variable to simplify searching a LUT. Identifying the inverse $g(\cdot)$ tends to be numerically and computationally challenging to obtain. In applications where the current is estimated using an observer instead of directly measured, $g(\cdot)$ is required to convert an estimated flux to an estimated current [12], [17]. In advanced controllers that use state space equations, the output equation is typically $g(\cdot)$ (5b).

This research proposes to express the WRSM magnetic model as a PWA map. PWA maps divide a nonlinear map into M domains (this process is described in Section IV) over which the function is linearized [25]. Hence we express the PWA current to flux map

$$\lambda = f(i) \approx f_{\mathrm{PWA}}(i) = \begin{cases} \mathbf{L}_1 i + \psi_1, & i \in \mathcal{I}_1, \\ \mathbf{L}_2 i + \psi_2, & i \in \mathcal{I}_2, \\ \quad \cdots & \\ \mathbf{L}_M i + \psi_M, & i \in \mathcal{I}_M, \end{cases} \tag{8}$$

where $\lambda = \mathbf{L}_j i + \psi_j$ is the affine equation that maps currents $i \in \mathcal{I}_j$ onto fluxes $\lambda \in \Lambda_j$ and Λ_j is the image of the domain $\mathcal{I}_j$. The affine map is defined by the the inductance matrix $\mathbf{L}_j$ and a flux offset ψ_j. Visualizations of $f_{\mathrm{PWA}}(i)$ are shown in Fig. 3. The process to calculate $\mathbf{L}_j$ and ψ_j is described in Section III.

The inverse of $f(\cdot)$ is

$$i = g(\lambda) \approx g_{\mathrm{PWA}}(\lambda) = \begin{cases} \mathbf{L}_1^{-1}(\lambda - \psi_1), & \lambda \in \Lambda_1, \\ \mathbf{L}_2^{-1}(\lambda - \psi_2), & \lambda \in \Lambda_2, \\ \quad \cdots & \\ \mathbf{L}_M^{-1}(\lambda - \psi_M), & \lambda \in \Lambda_M, \end{cases} \tag{9}$$

such that $i = g \circ f(i)$.

Each subset is defined to be be a simplex, which is the simplest possible polytope in any D-dimensional space and a tetrahetron in the three dimensions of the given problem. A D-dimensional simplex can be defined as the convex hull of its $D+1$ vertices (called the V-notation; alternatively, a simplex can be defined by its by its faces defined as affine inequalities called the H-notation [22])

$$\mathcal{I}_j = \mathcal{H}(\{i_{j_0}, i_{j_1}, \ldots, i_{j_D}\}), \tag{10}$$

where $i_{j_0}, \ldots, i_{j_D} \in \mathcal{I}_P$. Each current simplex $\mathcal{I}_j$ forms a domain of an affine map that maps into the flux simplex

$$\Lambda_j = \mathcal{H}(\{\lambda_{j_0}, \lambda_{j_1}, \ldots, \lambda_{j_D}\}), \tag{11}$$

where $\lambda_{j_0}, \ldots, \lambda_{j_D} \in \Lambda_P$. The general position of the defining set of measurement points implies that the vertices of

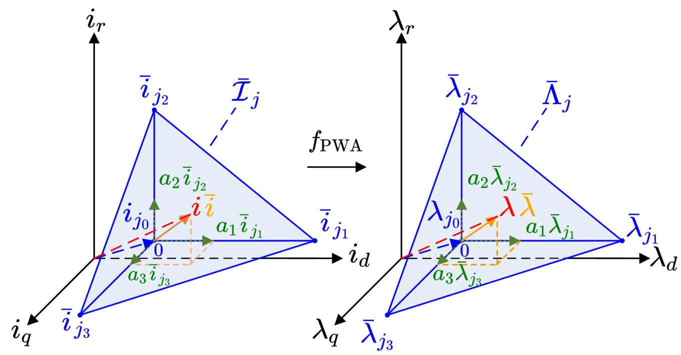

Fig. 6: Affine map visualization showing current simplex $\bar{\mathcal{I}}_j$ in dimension shifted by i_{j0} (left), and $\bar{\Lambda}_j$ in dimension shifted by λ_{j0} flux simplex (right).

each simplex are linearly independent and full dimension (not degenerate).

III. Identification of PWA Magnetic Maps

Each tetrahedron $\mathcal{I}_j$ is defined by four vertices shown in (10). Let one vertex i_{j_0} be the support vector such that we can move the origin $\bar{i} = i - i_{j_0}$. In the shifted dimension, the simplex is defined by

$$\bar{\mathcal{I}}_j = \mathcal{H}(0, \bar{i}_{j_1}, \ldots, \bar{i}_{j_D}\}), \tag{12}$$

where $\bar{i}_{j_k} = i_{j_k} - i_{j_0}$ $(k = \{1, \ldots, D\})$ span the simplex. Furthermore, we shift the flux space by the corresponding flux vector $\bar{\lambda} = \lambda - \lambda_{j_0}$ that results in the simplex

$$\bar{\Lambda}_j = \mathcal{H}(0, \bar{\lambda}_{j_1}, \ldots, \bar{\lambda}_{j_D}\}), \tag{13}$$

where $\bar{\lambda}_{j_k} = \lambda_{j_k} - \lambda_{j_0}$ $(k = \{1, \ldots, D\})$ span the simplex. The simplices $(D = 3)$ and the shift of origin are illustrated in Fig 6.

The nonzero vertices can be interpreted as a basis and since an affine map is an isomorphism, the relative position of a vector in the current and flux simplex is the same

$$\bar{i} = a_1 \bar{i}_{j_1} + \cdots + a_D \bar{i}_{j_D}. \tag{14}$$

The a coefficients can be obtained similar to how space vector modularion (SVM) computes relative on-times [25]. We project $\bar{i}$ onto the basis of $\bar{\mathcal{I}}_j$

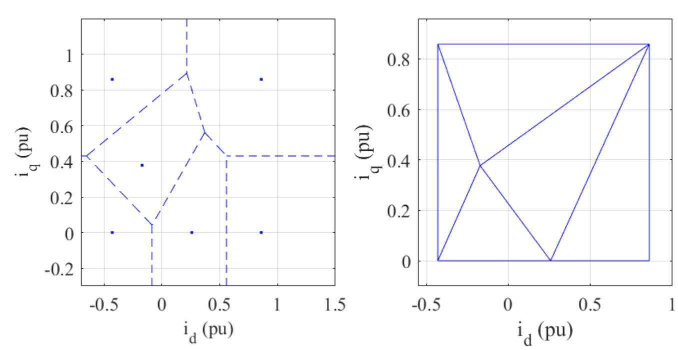

Fig. 7: Voronoi diagram (left) of a six-point irregular current grid in i_{dq} space (sliced at $i_r = 0$ pu); corresponding five-simplex Delauynay Triangulation (right)

$$p_{j_k} = \operatorname{proj}_{\bar{i}_{j_k}} \bar{i} = \frac{\bar{i}_{j_k} \cdot \bar{i}}{\|\bar{i}_{j_k}\|}, \tag{15}$$

and obtain the relative length of the vector by dividing the magnitude of the projections with the magnitude of the basis vectors

$$a_{j_k} = \frac{\|p_{j_k}\|}{\|\bar{i}_{j_k}\|}. \tag{16}$$

To find the flux vector $\bar{\lambda}$, we multiply a_k with the basis vectors of $\bar{\Lambda}_j$

$$\bar{\lambda} = a_1 \bar{\lambda}_{j_1} + \cdots + a_D \bar{\lambda}_{j_D}. \tag{17}$$

Then, the motor flux results from shifting the origin.

The steps (14) to (17) can be simplified using vector notation. Let the bases of $\bar{\mathcal{I}}_j$ and $\bar{\Lambda}_j$ be the matrices

$$\mathbf{M}_{\bar{\mathcal{I}}_j} = \left[\bar{i}_{j_1}, \ldots, \bar{i}_{j_D}\right], \tag{18a}$$
$$\mathbf{M}_{\bar{\Lambda}_j} = \left[\bar{\lambda}_{j_1}, \ldots, \bar{\lambda}_{j_D}\right], \tag{18b}$$

and $a = [a_1, \ldots, a_D]^T$. Then, we obtain $\bar{i} = \mathbf{M}_{\bar{\mathcal{I}}_j} a$ and $\bar{\lambda} = \mathbf{M}_{\bar{\Lambda}_j} a$ from (14) and (17). Since the simplices are not degenerate, the bases are nonsingular and we obtain the linear relationship

$$\mathbf{M}_{\bar{\Lambda}_j}^{-1} \bar{\lambda} = \mathbf{M}_{\bar{\mathcal{I}}_j}^{-1} \bar{i}, \tag{19}$$

that can be used to map current to flux and vice versa.

We can now substitute the original coordinates

$$\mathbf{M}_{\bar{\Lambda}_j}^{-1} (\lambda - \lambda_{j_0}) = \mathbf{M}_{\bar{\mathcal{I}}_j}^{-1} (i - i_{j_0}), \tag{20}$$

that result in the affine map

$$\lambda = \mathbf{L}_j i + \psi_j, \tag{21}$$

where $\mathbf{L}_j = \mathbf{M}_{\bar{\Lambda}_j} \mathbf{M}_{\bar{\mathcal{I}}_j}^{-1}$ and $\psi_j = \lambda_{j_0} - \mathbf{L}_j i_{j_0}$.

IV. Identification of PWA Magnetic Domains: Delaunay Triangulation

Constructing the PWA functions implies splitting the domain $\mathcal{I}$ and image Λ into M subdomains $\mathcal{I}_j$ and subimages Λ_j. We require that these subdomains are connected and that the resulting maps are non-conflicting. In other words, a point $i \in \mathcal{I}$ can be in one or more subdomains if and only if they map to the same point $\lambda \in \Lambda$. Hence, the domain can be split into simplices that do not overlap except for the border. Any point on the border $i \in \partial\mathcal{I}_j$ is expected to be part of two or more subdomains to ensure continuity. They all map onto the same $\lambda \in \partial\Lambda_j$ that is also part of two or more subdomains. In contrast, all points in the interior of the subdomains are part of only one subdomain.

In practice, the map is defined by a set of measured [6]–[8], [11], [13]–[16], simulated [8], [11], [16], or estimated [12], [17] current points $\mathcal{I}_P$ and flux points Λ_P. The convex hull of $\mathcal{I}_P$ and Λ_P is a reasonable domain $\mathcal{I}$ and image λ, respectively.

Subdomains are obtained by identifying unique and connected simplices using the Delaunay triangulation $\mathrm{DT}(\mathcal{I}_P)$ [26]. To calculate the Delaunay triangulation for $\mathcal{I}_P$, first a Voronoi diagram must be constructed using $\mathcal{I}_P$. The Voronoi diagram of $\mathcal{I}_P$ splits the $\mathcal{I}$ space into $|\mathcal{I}_P|$ Voronoi cells; all points in a Voronoi cell are closer to a single point in $\mathcal{I}_P$ than any other. To obtain the Delaunay triangulation, one may find the dual of the Voronoi diagram. A simple 2D example using dq currents is shown in Fig. 7. The Delaunay triangulation $\mathrm{DT}(\mathcal{I}_P)$ of the Euclidian space $\mathcal{I}$ guarantees that no point $i \in \mathcal{I}$ is inside two simplices in $\mathrm{DT}(\mathcal{I}_P)$. In general, $\mathrm{DT}(\mathcal{I}_P)$ is unique and there exists no set of $D+2$ points wherein one of the points lies strictly inside the minimally enclosing hypersphere of the point set. Each simplex or subdomain will have an affine equation, where the coefficients are calculated using (12)-(21) in Section III. The combination of subdomains and coefficients yields the PWA MM which has the form (8).

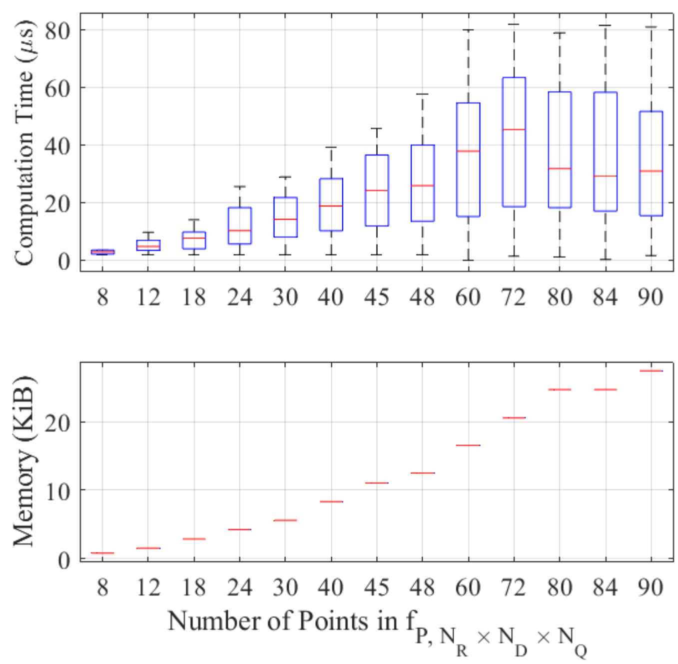

Fig. 8: DSP Evaluation: Computation time (μs) distribution vs Number of Points used in PWA (top), Memory (KiB) vs Number of Points used in PWA (bottom)

V. Static Evaluation with FEA Data

The data points $\mathcal{I}_P$ and Λ_P used to describe the flux-current map can be a regularly spaced grid, random data points, or data points selected to minimize the memory requirements considering the accuracy of the PWA function. Let $\mathcal{I}_{P,N_R \times N_D \times N_Q}$ denote a regularly spaced grid with N_R, N_D, and N_Q individual grid line current values in the r-axis, d-axis, and q-axis, respectively. The corresponding flux points are denoted as $\Lambda_{P,N_R \times N_D \times N_Q} = f \circ \mathcal{I}_{P,N_R \times N_D \times N_Q}$. A regularly gridded current space results in an irregular flux grid in general as it is shown in Fig. 4.

Throughout this section, the accuracy of the MM $f_{\mathrm{PWA}}(\cdot)$ (abbreviated f_{P}) with varying characteristics is benchmarked against a high fidelity MM spline interpolated $f_{S,44\times31\times42}$ ($f_s(\cdot)$ denoting spline interpolation),

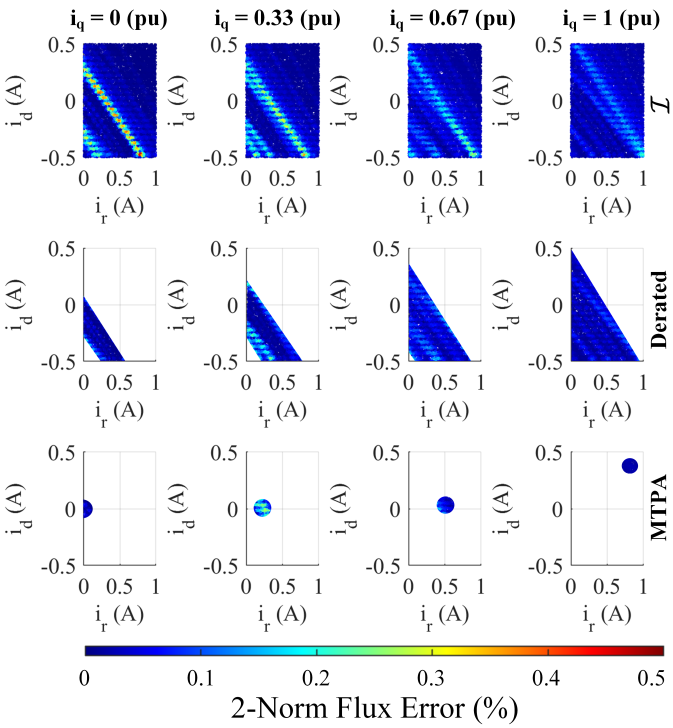

Fig. 9: Flux error distribution between high resolution MM: $f_{S,44\times31\times42}$ and $f_{P,44\times31\times42}$ at (left) $i_q = 0$ pu, (middle) $i_q = 0.4$ pu, (right) $i_q = 0.8$ pu; (top) full current domain, (middle) derated region, (bottom) MTPA trajectory

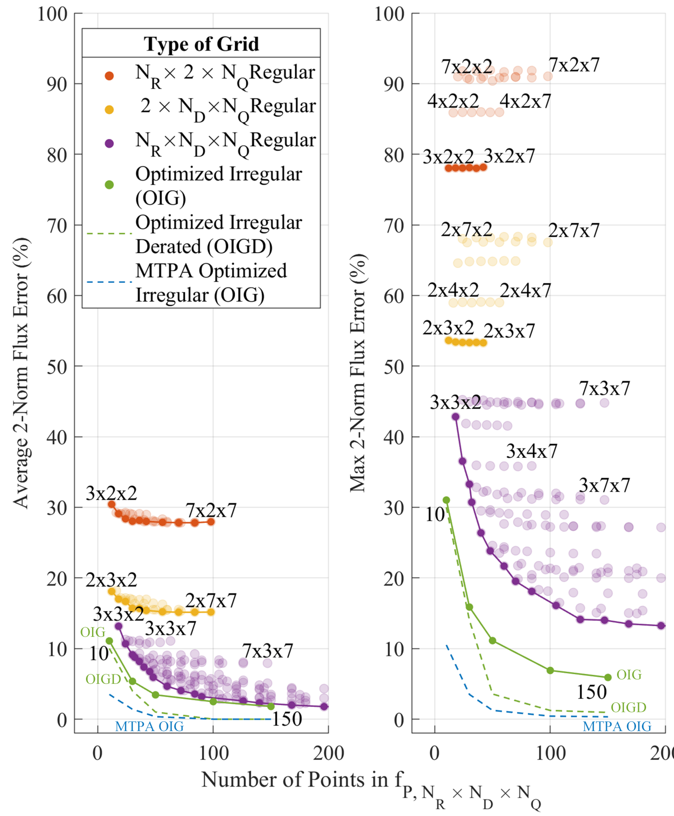

Fig. 10: Average 2-Norm flux error between variously sized $f_{P,N\times N\times N}$ (PWA interpolated) MMs and several optimized irregular gridded (PWA interpolated) MMs vs high fidelity $f_{S,44\times31\times42}$ (spline interpolated) MM

characterized by $\mathcal{I}_{S,44\times31\times42}$ and $\Lambda_{S,44\times31\times42}$. The datapoints $\mathcal{I}$ and Λ were obtained using FEA-analysis; the PWA interpolation is performed by creating subdomains using the process described in Section IV, then the coefficients of the affine function $f_{\mathrm{P}}(i)$ for each subdomain is computed using (12)-(21) in Section III.

The average 2-Norm flux error between the $f_{S,44\times31\times42}$ model and an arbitrary $f_{P,N_R\times N_D\times N_Q}$ model is computed by taking a large number of randomly selected points in the current space $\mathcal{I}$, computing the 2-Norm flux error of each point, then taking the average all errors.

The results for the error between $f_{S,44\times31\times42}$ and $f_{P,44\times31\times42}$ is shown in Fig 9. It is observed that error is the highest ($\approx 0.4\%$) in the most nonlinear regions of f, which occur along two diagonal lines across the i_r and i_d axis due to magnetic cross coupling (see Fig. 2).

The error for varying sized $f_{P,N_R\times N_D\times N_Q}$ are shown in Fig. 10, where all combinations between $f_{P,2\times2\times2}$ and $f_{P,7\times7\times7}$ are shown. As the number of grid lines in any axis increases, the average 2-Norm flux error generally stays the same or decreases. For the specific cases where $N_R = 2$ and $N_D = 2$, the average 2-Norm flux error saturates even as the number of grid lines in other axis are increased.

There may arise cases where we wish to decrease the number of data points $\mathcal{I}$ used in the mesh; we wish to select only the "important" points that decrease error the most. An optimized irregular grid (OIG) is created for this purpose to specifically minimize the maximum absolute error for a given number of datapoints.

An algorithm to create the OIG is shown in Fig. 11. The PWA MM obtained from using this optimized irregular grid, $f_{\mathrm{P,OIG(N)}}$ (where N is the total number of points used in the grid), reduces the average 2-Norm flux error by $1-15\%$ and maximum 2-Norm flux error by $9-20\%$. Points and pareto frontiers for error are shown in Fig. 10.

Other irregular grids of datapoints can be used to create a MM that minimizes error in specific regions of operation, instead of overall maximum error of the OIG described above. These regions could include maximum torque per ampere (MTPA) [27]), field weakening (FW), maximum torque per volt (MTPV), or other trajectories of the machine. Step three in the algorithm shown in Fig. 11 can be changed to only include points within a certain desired region or regions (instead of any random operating point), which will create an error-optimized grid for the desired region or regions. The error distribution for an OIG along the MTPA trajectory is shown in Fig. 9, and the total error is shown in Fig. 10. In derated operation, currents are limited to the unsaturated flux region (where flux error and copper losses are low), shown in Fig. 9. The average and max flux error of a derated drive will subsequently decrease, shown in Fig. 10 as OIG-derated (OIGD).

$f_{\mathrm{PWA}}(\cdot)$ of various sizes were tested on a Texas Instruments TMS320F28379D real-time microcontroller. The amount of memory used (KiB) and computation time (μs) increase nonlinearly with the number of data points

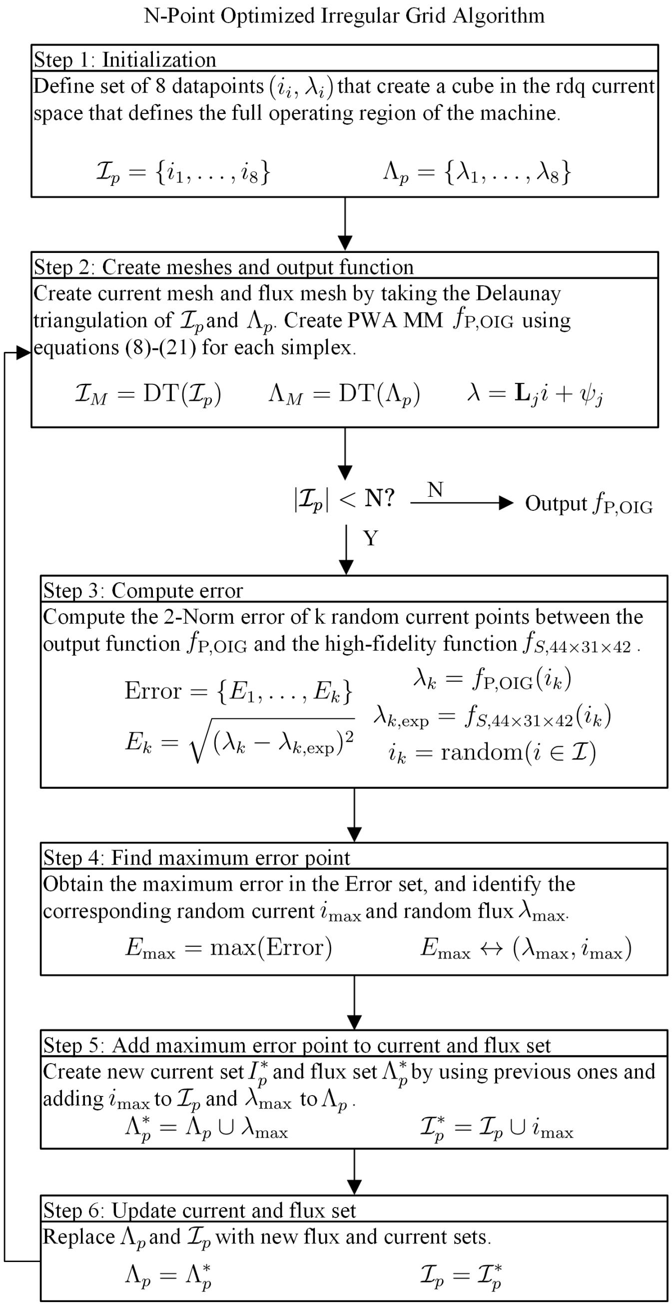

Fig. 11: Algorithm describing how to obtain a MM $f_{\mathrm{P,OIG(N)}}$ using an optimized irregular (not regularly gridded) grid of N points points, in the rdq current domain

used, but are in suitable range for machine controllers ($< 40\,\mu$s) (< 10 KiB) even at relatively high fidelity (using 40 datapoints), shown in Fig. 8. Warm starting and early termination are not used in computation timing, these methods may be be able to decrease online computation times by up to two orders of magnitude [28].

The number of points to use in the PWA MM depends on the machine application and controller type used. There are trade-offs between error, computation time, and memory. For example, if using the Texas Instruments TMS320F28379D, for an application where extremely low error is required one may choose an optimized irregular PWA MM with 150 points ($f_{\mathrm{P,OIG(150)}}$), so that the average error is $< 3\%$ (see Fig. 10). The computation will be slow ($> 90\mu$s) and the memory used on the controller large (> 30 KiB) (see Fig. 8). Alternatively, for an application where fast computation or small memory usage is required, the number of points used will be lower, increasing the error.

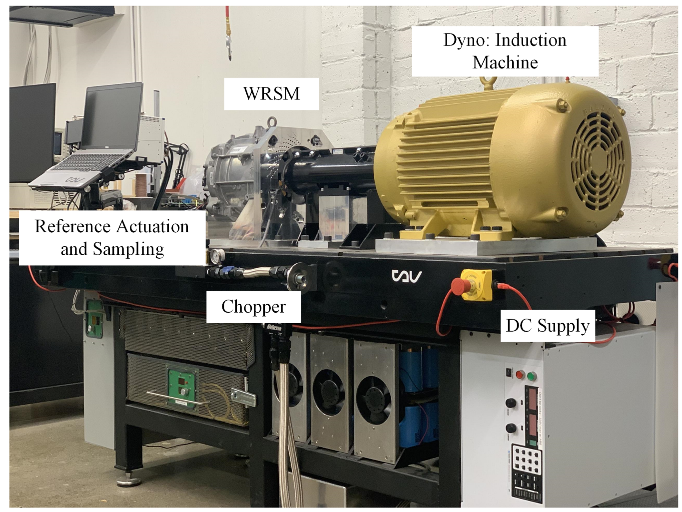

Fig. 12: WRSM bench setup: (clockwise from left) Reference Actuation and Sampling, WRSM, Dyno: Induction Machine, DC Supply, Chopper

VI. Testbench Validation

A simplified powertrain setup is shown in Fig. 5. An inverter converts the DC bus voltage u_{dc} to three phase AC voltage u_{abc} and current i_{abc} to excite the stator windings. A DC/DC converter steps u_{dc} to a desired rotor field voltage u_r and rotor field current i_r to excite the rotor winding. A WRSM was tested on a bench setup using a simple virtual-flux PI controller, TABLE II shows the parameters of the machine, and Fig. 1 shows a cross section of the machine. Current in the rotor axis is referred to the stator throughout this section.

A. Steady State Behavior

The accuracy of the proposed state space model (1) and the PWA MM (8) was evaluated by comparing ex-

TABLE II: WRSM Motor Drive Parameters

Parameter	Value
Turns ratio N_f/N_s	39
Pole pairs p	2
Stator resistance R_s	11.732 mΩ
Rotor resistance (stator referred) R_r	5.461 mΩ
Shaft inertia	22.76E-3 kg m^2
Switching frequency	10 kHz
Sampling frequency	20 kHz
Nameplate r-axis inductance L_r	1.956 mH
Nameplate d-axis inductance L_d	2.420 mH
Nameplate q-axis inductance L_q	0.789 mH
DC-link voltage u_{dc}	325 V
Rated power	65 kW
Rated torque	220 Nm
Base speed	3000 1/min

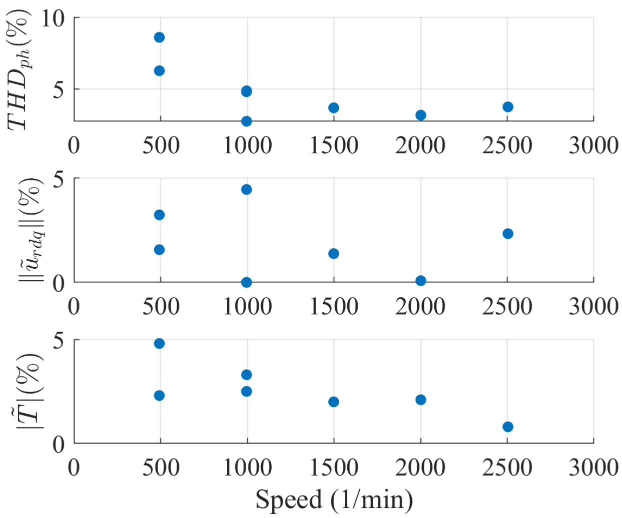

Fig. 13: PWA MM built using 60 points ($f_{P,4\times5\times3}$) (Top) mean THD across three phase currents, (Middle) error between experimental and expected voltage vs speed, (Bottom) error between experimental and expected torque vs speed

perimental and expected voltages and torques at steady state speeds. Voltage can be calculated by solving (1) at steady state speeds ($\dot{\lambda}_{rdq} = 0$), where terminal voltages become constant. Substituting (8) into (2), the torque of the machine becomes a function of only current that includes the MM,

$$T = pi'\mathbf{J}f_{\mathrm{PWA}}(i). \tag{22}$$

Thus by measuring the experimental torque and evaluating (22), the accuracy of f_{PWA} can be attained.

The results for static evaluation of a medium-sized PWA MM built using 60 points ($f_{P,4\times5\times3}$) are shown in Fig. 13 for speeds ranging from .167 pu to .835 pu. Voltage and torque error are kept below 5%, in accordance to what is expected from Fig. 10.

The state space model and PWA MM are shown to be robust against space and time harmonics in Fig. 13. The mean THD of the three-phase currents ($\mathrm{THD_{ph}}$) captures any deviation from the pure sinusoidal currents that occur at constant speed and constant load, which are caused by inverter switching non-linearities, slotting effects, and other non-ideal behaviors. Over a wide range of speeds the mean THD is between $2-10\%$, yet voltage and torque error remains below 5% in accordance to Fig. 10. At higher speeds the torque and voltage error tend to decrease due to nonlinear sensor characteristics and mechanical resonances.

B. Transient Behavior

Two time-domain experiments were conducted to verify the accuracy of the proposed PWA model in a dynamic setting. The results are shown in Fig. 14. and Fig. 15.

In the first experiment the WRSM is spun at a fixed speed of 1000 1/min using a coupled industrial drive. The WRSM exerts .5 - 44 Nm variable torque steps that follow torque references over a 120s period. The experiment shows how the accuracy of the proposed PWA MM behaves under abrupt steps, where the three-dimensional current vector rapidly travels through many PWA subdomains.

The second experiment is an automotive drive cycle. In this experiment the WRSM is acting as the motor for a vehicle, while the coupled industrial drive simulates the drivetrain and inertia of the vehicle. In this experiment the drive follows a 120s variable speed reference simulating the vehicle speeding up ($\approx +40$ Nm), slowing down (≈ -40 Nm), twice, with the vehicle coasting at around 1200 1/min in the first cycle. This experiment explores the error from the PWA MM functions over a wide range of speeds and torques.

In both experiments, the experimental results were evaluated offline using PWA MM of three resolutions: high fidelity spline ($f_{S,44\times31\times42}$), 90-point regular grid ($f_{P,5\times6\times3}$), and 90-point optimized irregular grid ($f_{\mathrm{P,OIG(90)}}$). These 90-point MMs were chosen as they put the controller to the limit in time and memory (see Fig. 8). The 2-Norm average error and error over time between the 90-point grid MMs and spline MM was evaluated. The MMs perform up to or better than the expected results found in simulation (Fig. 10), with flux error staying below 2% maximum and 1% average.

The torque was approximated offline using the measured current i, flux λ from the 90-point PWA MM $f_{\mathrm{P,OIG(90)}}$, and (22). This was compared to reference torque T^* in the first experiment and torque using flux λ from $f_{S,44\times31\times42}$ in the second experiment. In both cases the error does well, staying below 2.5% maximum and 1% average.

VII. Conclusion

A novel approach to modelling a machine's magnetic model for a controller using Piecewise Affine functions has been described and formalized. Static evaluation against other magnetic models shows high performance while maintaining desirable qualities for advanced linear state space control. Error and memory constraints were evaluated on a DSP demonstrating that an optimized irregular PWA function exceeds the accuracy of regularly gridded Look-up Tables (LUT) by 1% to 15% (average error) and 9% to 20% (peak error). A 40-point PWA MM has $< 40\mu$s computation time and uses < 10 KiB of space.

Evaluation of the PWA MM was tested on WRSM bench setup using a virtual flux controller, showing proficient results: $< 2\%$ maximum and average flux error over a wide range of speeds, torques, and current combinations. The new state space model was experimentally verified to $< 5\%$ error even in the presence of significant phase current harmonics.

Acknowledgment

The authors thank Michael Eull and Nick Vazquez for their support in developing simulation and data tools.

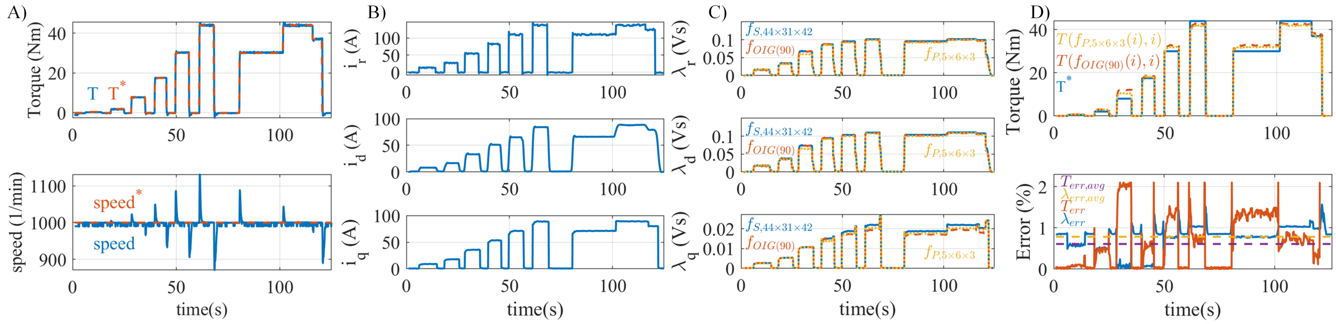

Fig. 14: 120s experimental transient PWA results: Torque steps (.5 - 44 Nm) at reference 1000 1/min speed, Left to right: **A) Experimental Result:** reference and measured torque T, reference and measured speed; **B)** measured currents i (rdq); **C) Estimated parameters:** PWA-approximated flux λ (rdq) in three resolutions (high fidelity spline, 90-point regular grid, 90-point irregular optimized grid); **D) Comparison:** (top) calculated torque T using (22) and reference torque T^*, (bottom) torque and flux error (flux error between PWA-approximated fluxes λ and high fidelity spline PWA flux λ)

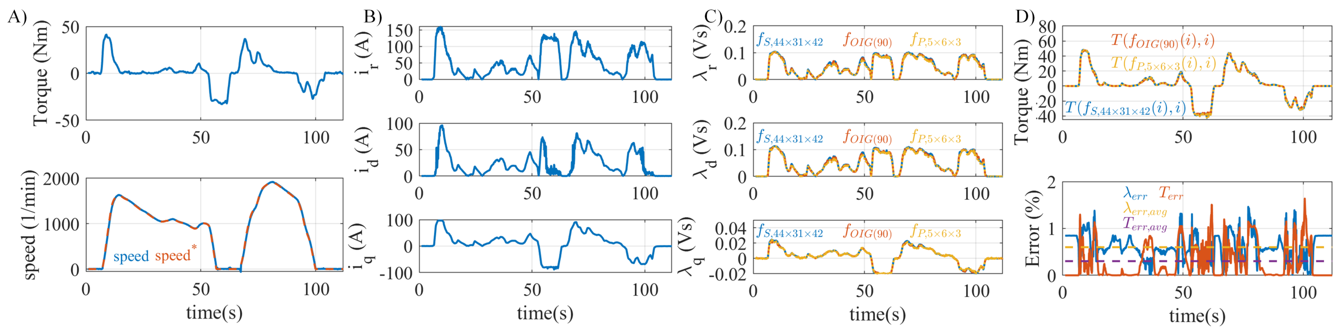

Fig. 15: 120s experimental transient PWA results: Automotive drive cycle (0 - 1910 1/min speed) exhibiting positive and negative torques, Left to right: **A) Experimental Result:** reference and measured speed, measured torque T; **B)** measured currents i (rdq); **C) Estimated parameters:** PWA-approximated flux λ (rdq) in three resolutions (high fidelity spline, 90-point regular grid, 90-point irregular optimized grid); **D) Comparison:** (top) calculated torques using (22), (bottom) torque and flux error (flux error between PWA-approximated fluxes λ and high fidelity spline PWA flux λ, PWA approximated torque T and calculated torque T using high fidelity spline PWA as reference)

References

[1] A. Dòria-Cerezo, C. Batlle, and G. Espinosa-Pérez, "Passivity-based control of a wound-rotor synchronous motor," *IET Control Theory & Appl.*, vol. 4, pp. 2049–2057, 2010.

[2] C. Rossi, D. Casadei, A. Pilati, and M. Marano, "Wound Rotor Salient Pole Synchronous Machine Drive for Electric Traction," in *Conf. Rec. IEEE Ind. Appl. Conf., IAS Annu. Meet.*, vol. 3, pp. 1235–1241, Oct. 2006, iSSN: 0197-2618.

[3] A. Doria-Cerezo, V. I. Utkin, R. S. Munoz-Aguilar, and E. Fossas, "Control of a Stand-Alone Wound Rotor Synchronous Generator: Two Sliding Mode Approaches via Regulation of the d-Voltage Component," *IEEE Trans. Control Syst. Technol.*, vol. 20, no. 3, pp. 779–786, May. 2012.

[4] J. de Santiago, H. Bernhoff, B. Ekergard, S. Eriksson, S. Ferhatovic, R. Waters, and M. Leijon, "Electrical Motor Drivelines in Commercial All-Electric Vehicles: A Review," *IEEE Trans. Veh. Technol.*, vol. 61, no. 2, pp. 475–484, Feb. 2012.

[5] A. Di Gioia, I. P. Brown, Y. Nie, R. Knippel, D. C. Ludois, J. Dai, S. Hagen, and C. Alteheld, "Design and Demonstration of a Wound Field Synchronous Machine for Electric Vehicle Traction With Brushless Capacitive Field Excitation," *IEEE Trans. Ind. Appl.*, vol. 54, no. 2, pp. 1390–1403, Mar. 2018.

[6] N. Bedetti, S. Calligaro, and R. Petrella, "Stand-Still Self-Identification of Flux Characteristics for Synchronous Reluctance Machines Using Novel Saturation Approximating Function and Multiple Linear Regression," *IEEE Trans. Ind. Appl.*, vol. 52, no. 4, pp. 3083–3092, Jul. 2016.

[7] H. Chen, C. Sun, and Q. Wang, "Analysis of Flux-Linkage Characteristics of Switched Reluctance Linear Generator," *IEEE Trans. Appl. Supercond.*, vol. 24, no. 3, pp. 1–5, Jun. 2014.

[8] H. Chen, W. Yan, and Q. Wang, "Electromagnetic Analysis of Flux Characteristics of Double-Sided Switched Reluctance Linear Machine," *IEEE Trans. Appl. Supercond.*, vol. 26, no. 4, pp. 1–7, Jun. 2016.

[9] P. Haghgooei, B. Nahid-Mobarakeh, N. Takorabet, and D. Arab-Khaburi, "Online Stator Flux Estimation for a Wound Rotor Synchronous Machine (WRSM)," in *Ind. Appl. Soc. IEEE-IAS Annu. Meet.*, pp. 1–6, Oct. 2020, iSSN: 2576-702X.

[10] P. Haghgooei, E. Jamshidpour, N. Takorabet, D. Arab-khaburi, and B. Nahid-Mobarakeh, "Magnetic Model Identification of Wound Rotor Synchronous Machine Using a Novel Flux Estimator," *IEEE Trans. on Ind. Applicat.*, pp. 1–1, 2021.

[11] K. Liu, J. Feng, S. Guo, L. Xiao, and Z.-Q. Zhu, "Identification of Flux Linkage Map of Permanent Magnet Synchronous Machines Under Uncertain Circuit Resistance and Inverter Nonlinearity," *IEEE Trans. Industr. Inform.*, vol. 14, no. 2, pp. 556–568, Feb. 2018.

[12] Y. Nie, D. C. Ludois, and I. P. Brown, "Deadbeat-Direct Torque and Flux Control of Wound Field Synchronous Machine at Low Sampling to Fundamental Frequency Ratios," *IEEE Trans. Ind. Appl.*, vol. 55, no. 4, pp. 3813–3822, Jul. 2019.

[13] M. Seilmeier and B. Piepenbreier, "Identification of steady-state inductances of PMSM using polynomial representations of the flux surfaces," in *IECON - 39th Annu. Conf. IEEE Ind. Electron. Soc.*, pp. 2899–2904, Nov. 2013, iSSN: 1553-572X.

[14] E. Armando, R. I. Bojoi, P. Guglielmi, G. Pellegrino, and M. Pastorelli, "Experimental Identification of the Magnetic Model of Synchronous Machines," *IEEE Trans. Ind. Appl.*, vol. 49, no. 5, pp. 2116–2125, Sep. 2013.

[15] E. Armando, P. Guglielmi, G. Pellegrino, and R. Bojoi, "Flux linkage maps identification of synchronous AC motors under

controlled thermal conditions," in *2017 IEEE Int. Electr. Mach. Drives Conf. (IEMDC)*, pp. 1–8, May. 2017.

[16] Q. Wang, G. Zhang, G. Wang, C. Li, and D. Xu, "Offline Parameter Self-Learning Method for General-Purpose PMSM Drives With Estimation Error Compensation," *IEEE Trans. Power Electron.*, vol. 34, no. 11, pp. 11 103–11 115, Nov. 2019.

[17] M. Wlas, Z. Krzeminski, and H. A. Toliyat, "Neural-Network-Based Parameter Estimations of Induction Motors," *IEEE Trans. Ind. Electron.*, vol. 55, no. 4, pp. 1783–1794, Apr. 2008.

[18] X. Li and R. Kennel, "General Formulation of Kalman-Filter-Based Online Parameter Identification Methods for VSI-Fed PMSM," *IEEE Trans. Ind. Electron.*, vol. 68, no. 4, pp. 2856–2864, Apr. 2021.

[19] D. Uzel, V. Smidl, and Z. Peroutka, "Gradient descent maximum torque control up to the base speed of wound rotor synchronous motors," in *2017 IEEE Int. Conf. Mechatron.*, pp. 1–6, Dec. 2016.

[20] N. Yang, B. Nahid-Mobarakeh, A. Corne, and J.-P. Martin, "Multiple-vector-based predictive direct current control for a wound rotor synchronous machine drive," in *Ind. Appl. Soc. IEEE-IAS Annu. Meet.*, pp. 1–9, Oct. 2016.

[21] I. Canay, "Causes of discrepancies on calculation of rotor quantities and exact equivalent diagrams of the synchronous machine," vol. PAS-88, pp. 1114–1120.

[22] F. Borrelli, A. Bemporad, and M. Morari, "Predictive control for linear and hybrid systems," 2017.

[23] J. Retif, X. Lin-Shi, A. Llor, and F. Morand, "New hybrid direct-torque control for a winding rotor synchronous machine," in *2004 IEEE 35th Annual Power Electronics Specialists Conference (IEEE Cat. No.04CH37551)*, vol. 2, DOI 10.1109/PESC.2004.1355634, pp. 1438–1442 Vol.2, 2004.

[24] M. Preindl and S. Bolognani, "Optimal state reference computation with constrained mtpa criterion for pm motor drives," *IEEE Trans. Power Electron.*, vol. 30, no. 8, pp. 4524–4535, 2015.

[25] P. Samuel and S. Levy, *Projective Geometry*, ser. Undergraduate Texts in Mathematics. Springer New York, 1988.

[26] F. Aurenhammer, "Voronoi diagrams, a survey of a fundamental geometric data structure," *ACM Comput. Surv.*, vol. 23, no. 3, p. 345.405, Sep. 1991.

[27] B. Steyaert, E. Swint, W. W. Pennington, and M. Preindl, "Piecewise affine maximum torque per ampere for the wound rotor synchronous machine," in *2022 IEEE Transp. Electr. Conf. Expo (ITEC)*, pp. 356–363, 2022.

[28] Y. Wang and S. Boyd, "Fast model predictive control using online optimization," *IEEE Trans. Control Syst. Technol.*, vol. 18, no. 2, pp. 267–278, 2010.

Bernard Steyaert (S'21) received a B.A. in Pre-Engineering Ursinus College (*summa cum laude, salutatorian*), B.S. and M.S. in Electrical Engineering from Columbia University in 2019, 2020, and 2022 respectively. He is currently pursuing a Ph.D. in Electrical Engineering with the Motor Drives and Power Electronics Laboratory at Columbia University. Research interests include control optimization for motor drives, as well as grid technologies.

Ethan Swint (M'04) received B.Sc. in electrical and computer engineering from Baylor University (2002), M.Sc. in mechanical engineering from University of Texas-Austin (2004), and Ph.D in electrical engineering from Virginia Tech (2012). He has been involved in the design and implementation of motor drive systems in companies ranging from startup to blue-chip, prototype to high-volume production. Since his doctoral work on switched reluctance machines, his interests have been on the integrated design of motor drive components - machines, electronics, and controls. Previously, he worked on design and manufacturing of a high-efficiency linear machine at Mainspring Energy, lead the third-generation motor designs from concept to production at Tesla, and fast-turn design-to-production of PM machines for a variety of applications with diameters ranging from 7mm-450mm at Celeramotion. Presently, he works to lead the development of motor drive systems which improve power density, efficiency, durability, economics, and sustainability at Tau Motors.

W. Wesley Pennington (M'21) is an entrepreneur and scientist focused on the research, development, and progress of emerging, deep technology across transformational industries. Presently, he is the Founder and CEO of Tau Motors, Inc. where he leads the company to build advanced technologies for electrification and energy systems to enable the transition to a more sustainable future. Wesley has a background as a technologist across a number of disciplines from applied AI to bioengineering. Previously, he was appointed to the faculty of management at the Kelley School of Business and worked in early-stage venture to develop and commercialize innovations out of academic and laboratory settings. He received a B.Sc. in biodynamics, Cert. management and human organization (*cum laude*), M.Sc. in human factors and biomechanics, and is a Ph.D candidate in cognitive neuromotor control all at Indiana University, where he is currently on leave as he builds Tau.

Matthias Preindl (S'12-M'15-SM'18) received the B.Sc. degree in electrical engineering (*summa cum laude*) from the University of Padua, Italy, the M.Sc. degree in electrical engineering and information technology from ETH Zurich, Switzerland, and the Ph.D. degree in energy engineering from the University of Padua, in 2008, 2010, and 2014, respectively. He is currently Associate Professor of Power Electronic Systems in the Department of Electrical Engineering at Columbia University, USA. Prior to joining Columbia University in 2016, he was an R&D Engineer of Power Electronics and Drives at Leitwind AG, Italy (2010-2012), a Post Doctoral Research Associate with the McMaster Institute for Automotive Research and Technology, McMaster University, Hamilton, ON, Canada (2014-2015), and a Sessional Professor in the Department of Electrical and Computer Engineering, McMaster University (2015). He serves as the area editor of vehicular electronics and systems at the IEEE Transactions on Vehicular Technology and as the general chair of the 2022 IEEE/AIAA ITEC+EATS. He received several awards and honors including the Horiba Awards Honorable Mention (Japan, 2019), the Futura Foundation Award (Italy, 2017), the NSF CAREER Award (USA, 2017), and he is the co-recipient of several best paper and presentation recognitions including the 2019 IEEE Transactions on Industrial Electronics best paper award.